POLITECNICO DI TORINO
Repository ISTITUZIONALE

Low Melting Non-corrosive Asymmetric Thioether-TFSI Li Salts for Solid Polymer Electrolytes

Original
Low Melting Non-corrosive Asymmetric Thioether-TFSI Li Salts for Solid Polymer Electrolytes / Shevtsov, V.Y., Gambino, F., Nosov, D.R., Guillot, J., Porporato, S., Elia, G.A., Gerbaldi, C., S Shaplov, A.. - In: CHEMICAL COMMUNICATIONS. - ISSN 1359-7345. - 62:39(2026), pp. 9922-9926. [10.1039/d6cc00051g]

Availability:
This version is available at: 11583/3010355 since: 2026-04-28T13:14:12Z

Publisher:
Royal Society of Chemistry

Published
DOI:10.1039/d6cc00051g

Terms of use:

This article is made available under terms and conditions as specified in the corresponding bibliographic description in the repository

Publisher copyright

(Article begins on next page)

30 October 2026

ChemComm

COMMUNICATION

View Article Online
View Journal

Check for updates

Cite this: DOI: 10.1039/d6cc00051g

Received 8th January 2026,
Accepted 14th April 2026

DOI: 10.1039/d6cc00051g

rsc.li/chemcomm

Open Access Article. Published on 27 April 2026. Downloaded on 5/21/2026 9:51:33 AM.
This article is licensed under a Creative Commons Attribution 3.0 Unported Licence.

Low melting non-corrosive asymmetric thioether-TFSI Li salts for solid polymer electrolytes

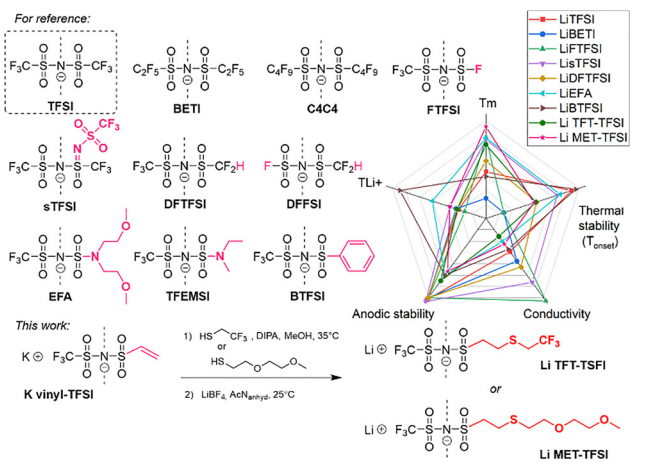
Vladislav Y. Shevtsov, †[ab] Francesco Gambino, †[cd] Daniil R. Nosov, [a] Jérôme Guillot, [e] Silvia Porporato, [cd] Giuseppe A. Elia, [cd] Claudio Gerbaldi *[cd] and Alexander S. Shaplov *[a]

High crystallinity in PEO-based solid polymer electrolytes limits ion transport and stability in Li-metal batteries. Two asymmetric, low-melting thioether-TFSI Li salts were synthesized *via* a thiol–ene route and incorporated into PEO. They suppress crystallinity while maintaining conductivity and electrochemical performance, and reduce Al corrosion *via* stable passivation layer formation. The resulting SPEs have improved Li compatibility and enable stable Li||$LiFePO_4$ cells cycling with high capacity retention and coulombic efficiency.

The market for portable electronics, including mobile phones, laptops, and remotely operated devices, is increasingly dominated by lithium-ion (Li-ion) and lithium-polymer (Li-Po) batteries based on liquid organic electrolytes. In contrast, lithium metal polymer (LiMP) batteries employ solid polymer electrolytes (SPEs), typically prepared by dissolving a Li salt in a polymer matrix, most commonly poly(ethylene oxide) (PEO). SPEs offer several advantages, including higher energy density, greater freedom in battery size, shape, and flexibility, and improved safety due to the absence or strongly reduced content of flammable organic solvents or plasticizers.[1]

Because safety is critical for market deployment, a major breakthrough was the introduction of lithium bis(trifluoromethylsulfonyl)imide (**LiTFSI**, Scheme 1), featuring a weakly coordinating, highly charge-delocalized $TFSI^-$ anion.[2] Weak coordination enhances Li^+ mobility, enabling high ionic conductivity (3.9×10^{-4} S cm^{-1} at 70 °C,[3] the typical operating temperature of LiMP batteries), together with excellent thermal and chemical stability, prompting efforts to replace the less thermally stable and more hazardous $LiPF_6$.[3–5] However, LiTFSI exhibits several well-known drawbacks in PEO-based SPEs (Table 1), including a low Li^+ transference number (T_{Li}^+ = 0.22),[6] lower ionic conductivity than $LiPF_6$/PEO systems,[7] poor long-term interfacial stability toward Li metal due to unstable SEI formation, and pronounced corrosion of aluminum current collectors.[4,8] These limitations have driven intensive research into $TFSI^-$ anion modification and the development of new weakly coordinating anions to achieve higher ionic conductivity, improved Li-anode interfacial stability, and better cycling performance with aluminum current collectors.[6,9–12] One promising strategy involves Li salts that are liquid at battery operating temperatures, as reduced melting points (T_m) can plasticize the PEO matrix, suppress crystallization, and broaden the operational temperature window of SPEs.

Early studies in this field examined how the length and symmetry of fluoroalkyl chains in TFSI-like anions affect the properties of Li salts and their SPEs (Scheme 1; *e.g.*, **LiBETI**,[13] **LiFTFSI**,[6] **LiC4C4**,[14] **LiC1C4**,[15] *etc.*). Increasing perfluoroalkyl chain length (**LiTFSI-LiBETI-LiC4C4**) was shown to improve SPE



Scheme 1 TFSI and asymmetric derivatives: reference structures and synthesis of thioether-TFSI Li salts.

[a] *Functional Polymeric and Particulate Materials Unit, Luxembourg Institute of Science and Technology (LIST), 28 avenue des Hauts-Fourneaux, L-4362 Esch-sur-Alzette, Luxembourg. E-mail: alexander.shaplov@list.lu*

[b] *Department of Physics and Materials Science, University of Luxembourg, 2, avenue de l'Université, L-4365 Esch-sur-Alzette, Luxembourg*

[c] *GAME Lab, Department of Applied Science and Technology (DISAT), Politecnico di Torino, Corso Duca degli Abruzzi 24, 10129 Torino, Italy. E-mail: claudio.gerbaldi@polito.it*

[d] *National Reference Center for Electrochemical Energy Storage (GISEL) - INSTM, Via G. Giusti 9, 50121, Firenze, Italy*

[e] *Advanced Analyses and Support Unit, Luxembourg Institute of Science and Technology (LIST), 28 avenue des Hauts-Fourneaux, L-4362 Esch-sur-Alzette, Luxembourg*

† V.Y.S and F.G. contributed equally to this work.

Open Access Article. Published on 27 April 2026. Downloaded on 5/21/2026 9:51:33 AM.
This article is licensed under a Creative Commons Attribution 3.0 Unported Licence.

Table 1 Thermal and electrochemical properties of Li salts and respective Li salt/PEO SPEs

	Neat Li salt		Li salt/PEO polyelectrolyte[a]		
Li salt	T_m[b] (°C)	T_{onset}[c] (°C)	σ 70 °C (S cm^{-1})	LSV[d] 70 °C (V)	T_{Li^+}[e] 70 °C
Li TFT-TFSI	136	240	2.1×10^{-4}	4.4	0.23
Li MET-TFSI	71	235	3.0×10^{-4}	4.1	0.29
For comparison:					
Li TFSI[6,14]	233	356	3.9×10^{-4}	4.6–5.1	0.22
Li BETI[13]	328	n.d	5.0×10^{-4}	n.d	0.24
Li C_4C_4[14]	352	334	2.2×10^{-4}	5.3	0.29
Li FTFSI[6]	110	150	9.7×10^{-4}	5.2	0.17
Li sTFSI[18]	118	300	7.5×10^{-4}	5.4	0.29
Li DFFSI[19]	n.d.	184	6.6×10^{-4}	n.d	0.23
Li DFTFSI[20]	194	242	5.7×10^{-4}	5.2	0.35
Li EFA[23]	112	308	2.7×10^{-4}	4.0	0.43
Li TFEMSI[24]	181	318	3.5×10^{-4}	n.d	0.64
Li BTFSI[11,25]	n.d.	352	3.6×10^{-4}	4.0	0.69

[a] The Li salts/PEO blends composition was fixed at [EO]/[Li^+] = 20 (note: PEO with different molecular weights may be used). [b] Melting point (T_m) determined by DSC under N_2 (note: heating rates of 5 or 10 °C min^{-1} may be employed). [c] Onset weight loss temperature determined by TGA in air (note: heating rates of 5 or 10 °C min^{-1} may be employed). [d] Anodic stability by linear sweep voltammetry (LSV) at 70 °C. [e] Li-ion transference number measured at 70 °C.

interfacial compatibility with both anode and cathode materials (Table 1).[14] However, this modification increased T_m of salts melting points, exerted opposing effects on ionic conductivity of Li salt/PEO materials, and does not enhance Li^+ transport, as highly fluorinated groups interact only weakly with PEG chains.[6,13,14,16] In contrast, introducing asymmetry into the TFSI anion substantially reduces T_m while improving other SPE properties.[17–20] Consequently, recent research has focused on asymmetric weakly coordinating anions, with several TFSI-type systems showing attractive features (Scheme 1). Lithium super-TFSI (**sTFSI**[17,18]) exhibits a markedly lower melting point (118 °C[18] *vs.* 233 °C for **LiTFSI**). This reduction, together with enhanced salt solubility, allows PEO SPEs to achieve approximately doubled ionic conductivity at 70 °C and a slightly increased T_{Li^+} without compromising electrochemical stability (Table 1).[18] However, stable cycling of Li||$LiFePO_4$ cells with **LisTFSI** has been demonstrated only in ionic liquid (IL) electrolytes, requiring combination with ILs such as [N-alkyl-N-methylpiperidinium$^+$ sTFSI$^-$].[21]

Building on anion asymmetry, several studies introduced a positive dipole into the anion structure, leading to **DFTFSI**[7,20,22] and **DFFSI**[19] anions, where one fluorine atom was replaced by hydrogen. This modification caused only a modest reduction in T_m of Li-salt; however, **LiDFTFSI/PEO**[20] and **LiDFFSI/PEO**[19] SPEs showed ~1.5 fold higher ionic conductivity than **LiTFSI/PEO**, reduced interfacial resistance, improved compatibility with metal Li, and strongly suppressed Al corrosion. **LiDFTFSI/PEO**[20] exhibited increased T_{Li^+} (0.22 to 0.35), attributed to $-CF_2H\cdots$PEO hydrogen bonding. As a result, **LiDFFSI/PEO** enabled Li||$LiFePO_4$ cycling at 70 °C for up to 125 cycles at C/10,[19] while **LiDFTFSI/PEO**, benefiting from higher anodic stability, supported Li||Li-S cells at similar rates, albeit with capacity fading.[22]

A related strategy combining anion asymmetry with stronger polymer interactions was applied in **EFA**[23] and **TFEMSI**[24] anions, where a tertiary amine is directly attached to the sulfonyl group. Incorporation of short PEG chains lowers the T_m of **LiEFA** to 112 °C (Table 1) and increases the T_{Li^+} to 0.43 *via* segmental entanglement and hydrogen bonding with PEO.[23] However, this design reduced electrochemical stability toward Li (≈4 V) and slightly lowered thermal stability.[23] Nevertheless, **LiEFA/PEO** SPEs enabled stable Li°||$LiFePO_4$ cycling for 30 cycles at C/3, attributed to (i) suppressed anion mobility, reducing concentration polarization and dendrite formation, and (ii) formation of a stable SEI that facilitates Li^+ transport across the interface.

To date, one of the highest Li^+ transference numbers reported for PEO-based SPEs (T_{Li^+}= 0.69) has been achieved using **LiBTFSI**.[25] This high selectivity was attributed to π–π stacking between anion-attached benzene rings, promoting anion self-aggregation and suppressing negative-charge mobility. While the total ionic conductivity of **LiBTFSI/PEO** is comparable to **LiTFSI/PEO**, its anodic stability is reduced to ~4.0 V, and aluminum corrosion was not evaluated.[25] Nevertheless, the SPE showed excellent compatibility with Li metal, enabling stable solid-state Li°||$LiFePO_4$ cycling with 86% capacity retention after 200 cycles at C/3 rate.

Despite these advances and other strategies, such as the incorporation of fillers,[26,27] simultaneously improving ionic conductivity in PEO-based SPEs and mitigating interfacial instability in LiMP batteries remains challenging, as gains often compromise Li^+ selectivity, thermal and electrochemical stability, moisture resistance, or aluminum compatibility. Moreover, reducing fluorine content in Li salts is increasingly important for large-scale deployment and regulatory compliance. To address the need for non-corrosive lithium salts with weakly coordinating anions, low T_m, and SPEs combining high ionic conductivity with elevated T_{Li^+}, we developed a simple synthetic strategy based on thiol–ene click chemistry (Scheme 1).[28] This approach uses commercially available potassium vinyl-TFSI[29] and enables modular access to a broad family of asymmetric anions through a two-step reaction with selected thiols. The method features operational simplicity, consistently high yields, facile product isolation, and high purity suitable for electrochemical applications.

In this work, vinyl-TFSI K was reacted with 2,2,2-trifluoroethanethiol and 2-(2-methoxyethoxy)ethane-1-thiol (Scheme 1). The former affords a minimal asymmetric anion bearing a fluorinated $-CH_2-CF_3$ group, while the latter introduces two ethylene oxide units expected to interact with PEO and reduce anion mobility. Subsequent cation exchange yielded the target thioether-TFSI lithium salts: lithium ((2-((2,2,2-trifluoroethyl)-thio)ethyl)sulfonyl)-*N*-(trifluoromethylsulfonyl)-imide (**Li TFT-TFSI**) and lithium ((2-((2-(2-methoxyethoxy)ethyl)thio)ethyl)-sulfonyl)-*N*-(trifluoromethylsulfonyl)imide (**Li MET-TFSI**). Structural integrity and purity were confirmed by ^1H, ^7Li, ^{13}C and ^{19}F NMR, IR spectroscopy, and elemental analysis (Fig. S1–S11, SI). 2D NMR experiments (HSQC, HMBC) enabled full proton and carbon assignment of **Li MET-TFSI** (Fig. S12 and S13, SI).

Differential scanning calorimetry (DSC) showed melting points (T_m, observed during the first heating) of 136 and 71 °C for **Li TFT-TFSI** and **Li MET-TFSI**, respectively (Fig. S14 and S15, SI), with the latter representing the lowest T_m reported for TFSI-type Li salts to date (Fig. 1a). This strong melting-point

 This journal is © The Royal Society of Chemistry 2026

Open Access Article. Published on 27 April 2026. Downloaded on 5/21/2026 9:51:33 AM.
This article is licensed under a Creative Commons Attribution 3.0 Unported Licence.

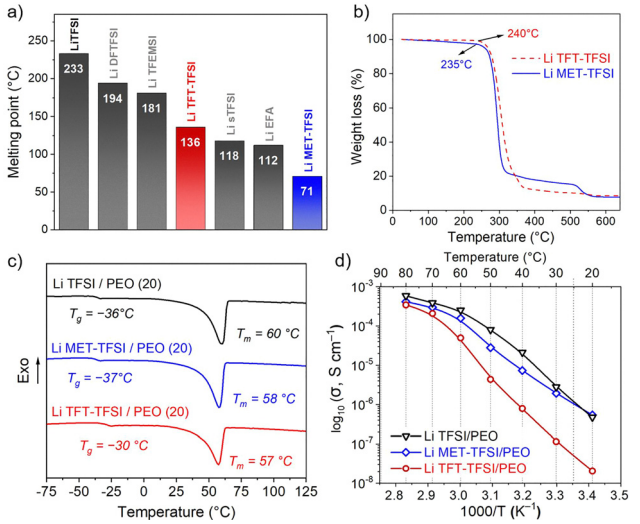


Fig. 1 Physical, thermal, and electrochemical properties of neat Li salts and LiX/PEO polyelectrolytes (X = TFT-TFSI, MET-TFSI, or TFSI; [EO/Li^+] = 20): (a) Summary of melting points of asymmetric sulfonimide Li salts; (b) TGA plots of neat Li salts in air; (c) DSC traces of polyelectrolytes; (d) Arrhenius plots of ionic conductivity *vs.* inverse temperature for polyelectrolytes determined by EIS in the range 20–80 °C.

reduction is attributed to the methoxyethoxy-thioethyl substituent, whose steric and conformational effects disrupt anion packing and suppress crystallization. Consistently, the second DSC cycle showed no crystallization upon slow cooling and only a glass transition ($T_g \approx -3.0$ °C) was detected. Thermogravimetric analysis (TGA) in air revealed an onset of weight loss above 235 °C (Fig. 1b), indicating sufficient thermal stability for practical application, as LiMP batteries typically operate below 100 °C.

Converting the Li salts into PEO-based SPEs with an [EO]/[Li^+] ratio of 20 yielded self-standing, semi-transparent membranes, whose thermal properties were analyzed by DSC (Fig. 1c and Fig. S16, S17, SI). Fig. 1c shows first-heating DSC traces of **Li TFT-TFSI/PEO** and **Li MET-TFSI/PEO** SPEs, benchmarked against **LiTFSI/PEO**. All samples exhibited a glass transition (T_g = −37.4 to −29.6 °C) and a PEO melting transition (T_m = 57.3–60.5 °C). The T_g values decrease in the order: −29.6 °C (**Li TFT-TFSI/PEO**) > −35.7 °C (**LiTFSI/PEO**) > −37.4 °C (**Li MET-TFSI/PEO**), indicating a stronger plasticizing effect of **Li MET-TFSI**. Analysis of the melting transition showed T_m values of 60.5 °C (**LiTFSI/PEO**) > 58.0 °C (**Li MET-TFSI/PEO**) > 57.3 °C (**Li TFT-TFSI/PEO**), consistent with melting enthalpies ΔH_m of 68.5, 66.2, and 54.1 J g^{-1}, respectively. These results demonstrate reduced PEO crystallinity in **Li MET-TFSI/PEO** and **Li TFT-TFSI/PEO** compared to **LiTFSI/PEO**. This reduction arises from both the lower intrinsic melting points of the new salts and their enhanced plasticizing efficiency. Additionally, suppressed PEO recrystallization can be attributed to the increased flexibility and larger substituents of the modified TFSI anions,[6,18,22] which enhance segmental mobility and hinder crystallization.

Fig. 1d presents Arrhenius plots of total ionic conductivity (σ), reflecting combined Li^+ and anion transport, for **Li TFT-TFSI/PEO**, **Li MET-TFSI/PEO**, and **LiTFSI/PEO** SPEs. In the near-ambient range (20–30 °C), **Li MET-TFSI/PEO** shows the highest conductivity (5.4×10^{-7} S cm^{-1}), exceeding **LiTFSI/PEO** (4.7×10^{-7} S cm^{-1}) and **Li TFT-TFSI/PEO** (2.0×10^{-8} S cm^{-1}). However, conductivities of all systems remain insufficient for LiMP batteries, mainly due to crystalline PEO domains that strongly impede ion transport. Upon heating above 60 °C, conductivity increased sharply for all SPEs, reaching ~10^{-4} S cm^{-1} (Fig. 1d), attributed to melting-induced amorphization of the PEO matrix that enables continuous ion-conducting pathways and enhances ion mobility.[1] At 70 °C, ionic conductivity increased with decreasing effective anion volume in the order (Table 1): 2.1×10^{-4} S cm^{-1} (**Li TFT-TFSI/PEO**) < 3.0×10^{-4} S cm^{-1} (**Li MET-TFSI/PEO**) ≤ 3.9×10^{-4} S cm^{-1} (**LiTFSI/PEO**).

To evaluate the suitability of thioether-TFSI lithium salts for application in LiMP batteries, the electrochemical properties of **Li TFT-TFSI/PEO** and **Li MET-TFSI/PEO** were systematically investigated with particular attention to the T_{Li}^+, anodic stability, compatibility with the Li metal electrode, and cycling performance in Li°||Li_x/PEO||$LiFePO_4$ (LFP) cells. The Li-ion transference number of the SPEs was determined using the Evans–Vincent–Bruce method (Fig. S18). Notably, **Li MET-TFSI/PEO** exhibited a higher T_{Li}^+ value (0.29) compared to **LiTFSI/PEO** (0.22) and **Li TFT-TFSI/PEO** (0.23). This enhanced T_{Li}^+ can be attributed to a combination of two effects: (i) increased mobility of Li^+-containing species resulting from the lower T_g of the SPE, enabled by the stronger plasticizing effect of **Li MET-TFSI**, and (ii) reduced mobility of the **MET-TFSI** anions due to their stronger interactions with the PEO matrix.

The linear sweep voltammograms (LSVs) of the SPEs are compared in Fig. 2a. All SPEs show anodic breakdown at ~4 V *vs.* Li/Li^+, attributed to oxidative degradation of the PEO matrix.[30] Increasing the potential to ~4.8 V resulted in a sharp rise in polarization current, indicating the onset of oxidative decomposition involving the thioether anions, possibly together with PEO. The oxidative stability of the Li salt/PEO blends at 70 °C follows the trend: Li TFSI (LSV = 4.6 V) > **Li TFT-TFSI** (4.4 V) > **Li MET-TFSI** (4.1 V). Nonetheless, both newly developed Li salts exhibit sufficient anodic stability for operation in LFP batteries. Anodic dissolution tests were performed using 1 M Li salt solutions in EC/DMC (1 : 1 v/v) with uncoated Al discs by holding the potential 1.3 V above the open-circuit potential of the corresponding half-cell (Fig. S19, SI). During first cycle, current densities of ~0.9 and ~0.1 μA cm^{-2} were recorded for **Li MET-TFSI** and **Li TFT-TFSI**, which are negligible compared to **LiTFSI**, for which a sustained current density of ~15 mA cm^{-2} was observed (Fig. S19). This pronounced response for **LiTFSI** clearly indicates anodic dissolution of the Al° current collector.[7] In contrast, the very low currents for **Li MET-TFSI** and **Li TFT-TFSI** are attributed to the formation of a highly resistive passivation layer on the Al surface, effectively suppressing anodic dissolution.[7,31,32] XPS analysis revealed increased Li- and F-rich species on Al after anodic dissolution in **Li MET-TFSI** and **Li TFT-TFSI** electrolytes, compared to **LiTFSI** (Fig. S20 and S21), indicating a more fluoride-rich interphase with higher LiF and AlF_3 content and improved corrosion protection (see SI). Strongly reduced corrosion was further confirmed by FESEM: severe pitting was observed for **LiTFSI** after cycling (Fig. S22, SI),[31] whereas no pitting features were detected on Al discs from **Li MET-TFSI** or **Li TFT-TFSI** electrolytes (Fig. S23 and S24, SI).

Open Access Article. Published on 27 April 2026. Downloaded on 5/21/2026 9:51:33 AM.
This article is licensed under a Creative Commons Attribution 3.0 Unported Licence.

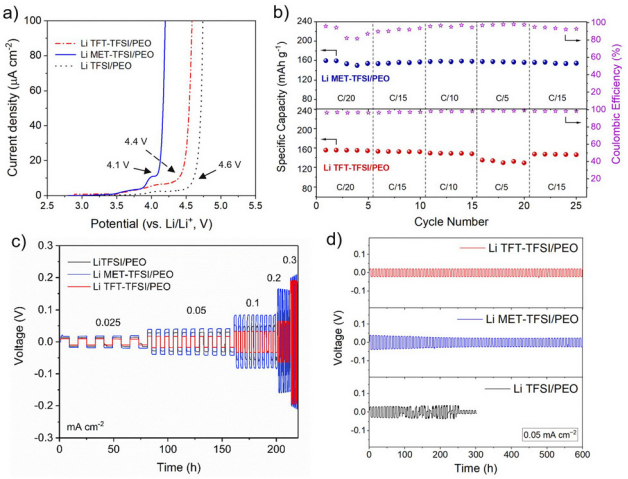


Fig. 2 Electrochemical behavior of **Li TFT-TFSI/PEO** (red), **Li MET-TFT/PEO** (blue), and **Li TFSI/PEO** (black) at 70 °C: (a) linear sweeping voltammetry profiles measured in a Li°||Li_x/PEO||Al carbon-coated configuration at a scan rate of 0.1 mV s^{-1}; (b) specific capacity and coulombic efficiency as a function of cycle number for Li°|| Li_x/PEO||$LiFePO_4$ cells at variable C-rates; (c) galvanostatic cycling of Li°||Li_x/PEO||Li° symmetric cells at different current densities (total plated/stripped capacity of 0.3 mAh cm^{-2} per half cycle); (d) long-term cycling performances of Li symmetric cell at 0.050 mA cm^{-2}.

Fig. 2b shows the discharge capacity as a function of current density (C/20, C/15, C/10, C/5, and back to C/15) for Li°||Lix/PEO||$LiFePO_4$ cells. SPEs based on **Li TFT-TFSI** and **Li MET-TFSI** display stable charge/discharge behavior across all C-rates, together with excellent cycling stability and high Coulombic efficiency. Both SPEs maintain capacities close to the theoretical value of $LiFePO_4$ ($\approx$160 mAh g^{-1}), with Coulombic efficiencies above 98% at all tested rates (Fig. 2b and S25–S27, SI), whereas the conventional **LiTFSI/PEO** electrolyte delivers significantly lower capacities of $\sim$130–140 mAh g^{-1} under identical conditions (Fig. S28 and S29, SI). Fig. 2c presents galvanostatic lithium plating/stripping in Li° symmetric cells at 70 °C and different current densities. While **LiTFSI/PEO** exhibits pronounced voltage instabilities already at 0.1 mA cm^{-2}, the TFT-TFSI- and MET-TFSI-based SPEs allow stable cycling at 0.2 mA cm^{-2} with lower overpotentials than the reference system. During long-term cycling at 0.05 mA cm^{-2} (Fig. 2d), the **Li TFT-TFSI/PEO** and **Li MET-TFSI/PEO** cells remained stable for over 600 h, whereas the LiTFSI-based cell short-circuited after $\sim$250 h, indicating markedly improved Li° electrode stability due to reduced concentration polarization and suppressed dendritic lithium growth. Moreover, **Li TFT-TFSI** and **Li MET-TFSI** SPEs sustain higher current densities compared to LiTFSI/PEO that short-circuits rapidly, as indicated by CCD tests (Fig. S30, SI).

In summary, two asymmetric thioether-TFSI lithium salts address key limitations of LiTFSI-based PEO electrolytes. Their low melting points suppress PEO crystallinity, enabling plasticization while maintaining ionic conductivity and Li^+ transference number. Both salts inhibit aluminum corrosion via the formation of stable passivation layer. In PEO-based SPEs, this yields improved Li compatibility and stable long-term Li||$LiFePO_4$ cells cycling with high capacity retention and Coulombic efficiency. The modular thiol–ene synthesis enables structural tunability with reduced fluorine content, supporting scalability and regulatory compliance.

Conflicts of interest

There are no conflicts to declare.

Data availability

The data supporting this article have been included as part of the supplementary information (SI). Supplementary information: materials and methods; full experimental details for the synthesis of **Li TFT-TFSI** and **Li MET-TFSI**, their ^1H, ^{13}C, ^{19}F, HSQC and HMBC NMR spectra, elemental analysis and DSC traces; synthesis of **Li MET-TFSI/PEO** and **Li TFT-TFSI/PEO** materials, their DSC traces, EIS and polarization current curves; anodic dissolution behavior of aluminum in 1 M Li salt in EC-DMC (1 : 1 v/v) liquid electrolytes; XPS analysis of aluminium disks after dissolution, specific capacity and coulombic efficiency as a function of cycle number for Li°||**Li TFT-TFSI/PEO**||$LiFePO_4$ and Li°||**Li MET-TFSI/PEO**||$LiFePO_4$ cells during galvanostatic cycling at C/15 and 70 °C as well as their potential *vs.* specific capacity profiles, and critical current density tests has been provided. See DOI: https://doi.org/10.1039/d6cc00051g.

Acknowledgements

This work was supported by Luxembourg National Research Fund (FNR) through FNRS-FNR project INFINITE (agreement no. INTER/FNRS/21/16555380/INFINITE), by the National Recovery and Resilience Plan under Next-GenerationEU (PIANO NAZIONALE DI RIPRESA E RESILIENZA – PNRR Mission 4, Component 2, Investment 1.4 and D.D. 1033 June 17, 2022 of the Ministero dell'Universitá e della Ricerca (MUR), CN00000023) and by the Italian MUR through the "Dipartimenti di Eccellenza 2023–2027" (CUPE17G22001490006) program.

References

1 Z. Xue, D. He and X. Xie, *J. Mater. Chem. A*, 2015, **3**, 19218–19253.
2 S. Callens, J.-F. Le Nest, A. Gandini and M. Armand, *Polym. Bull.*, 1991, **25**, 443–450.
3 A. Hammami, N. Raymond and M. Armand, *Nature*, 2003, **424**, 635–636.
4 J.-M. Tarascon and M. Armand, *Nature*, 2001, **414**, 359–367.
5 Q. Wang, P. Ping, X. Zhao, G. Chu, J. Sun and C. Chen, *J. Power Sources*, 2012, **208**, 210–224.
6 B. Tong, P. Wang, Q. Ma, H. Wan, H. Zhang, X. Huang, M. Armand, W. Feng, J. Nie and Z. Zhou, *Solid State Ion.*, 2020, **358**, 115519.
7 L. Qiao, U. Oteo, M. Martinez-Ibañez, A. Santiago, R. Cid, E. Sanchez-Diez, E. Lobato, L. Meabe, M. Armand and H. Zhang, *Nat. Mater.*, 2022, **21**, 455–462.
8 L. J. Krause, W. Lamanna, J. Summerfield, M. Engle, G. Korba, R. Loch and R. Atanasoski, *J. Power Sources*, 1997, **68**, 320–325.
9 G. Guzmán-González, M. Alvarez-Tirado, J. L. Olmedo-Martínez, M. L. Picchio, N. Casado, M. Forsyth and D. Mecerreyes, *Adv. Energy Mater.*, 2023, **13**, 2202974.
10 D. Flachard, J. Rolland, M. M. Obadia, A. Serghei, R. Bouchet and E. Drockenmuller, *Chem. Commun.*, 2018, **54**, 9035–9038.
11 M. B. Herath, S. E. Creager, R. V. Rajagopal, O. E. Geiculescu and D. D. DesMarteau, *Electrochim. Acta*, 2009, **54**, 5877–5883.
12 S. Bhowmick, M. Ahmed, A. Filippov, L. C. Loaiza, F. U. Shah and P. Johansson, *Chem. Commun.*, 2023, **59**, 2620–2623.
13 G. B. Appetecchi and S. Passerini, *J. Electrochem. Soc.*, 2002, **149**, A891.
14 B. Tong, Z. Song, W. Feng, J. Zhu, H. Yu, X. Huang, M. Armand, Z. Zhou and H. Zhang, *Adv. Energy Mater.*, 2023, **13**, 2204085.

Open Access Article. Published on 27 April 2026. Downloaded on 5/21/2026 9:51:33 AM.
This article is licensed under a Creative Commons Attribution 3.0 Unported Licence.

15 F. Castiglione, M. Moreno, G. Raos, A. Famulari, A. Mele, G. B. Appetecchi and S. Passerini, *J. Phys. Chem. B*, 2009, **113**, 10750–10759.
16 N. Nishi, Y. Yasui, T. Uruga, H. Tanida, T. Yamada, S. Nakayama, H. Matsuoka and T. Kakiuchi, *J. Chem. Phys.*, 2010, **132**, 164705.
17 H. Zhang, H. Han, X. Cheng, L. Zheng, P. Cheng, W. Feng, J. Nie, M. Armand, X. Huang and Z. Zhou, *J. Power Sources*, 2015, **296**, 142–149.
18 H. Zhang, Z. Song, W. Yuan, W. Feng, J. Nie, M. Armand, X. Huang and Z. Zhou, *ChemElectroChem*, 2021, **8**, 1322–1328.
19 L. García, D. Fraile-Insagurbe, I. Serna, I. Aldalur, L. Meabe, M. Arrese-Igor, R. Cid, J. Etxabe, M. Armand and M. Martinez-Ibañez, *Energy Environ. Mater.*, 2025, e70143.
20 H. Zhang, U. Oteo, H. Zhu, X. Judez, M. Martinez-Ibañez, I. Aldalur, E. Sanchez-Diez, C. Li, J. Carrasco, M. Forsyth and M. Armand, *Angew. Chem., Int. Ed.*, 2019, **58**, 7829–7834.
21 H. Zhang, X. Cheng, Q. Ma, W. Feng, L. Zheng, J. Nie, X. Huang, M. Armand and Z. Zhou, *Electrochim. Acta*, 2016, **207**, 66–75.
22 H. Zhang, U. Oteo, X. Judez, G. G. Eshetu, M. Martinez-Ibañez, J. Carrasco, C. Li and M. Armand, *Joule*, 2019, **3**, 1689–1702.
23 H. Zhang, F. Chen, O. Lakuntza, U. Oteo, L. Qiao, M. Martinez-Ibañez, H. Zhu, J. Carrasco, M. Forsyth and M. Armand, *Angew. Chem., Int. Ed.*, 2019, **58**, 12070–12075.
24 M. Martinez-Ibañez, E. Sanchez-Diez, U. Oteo, I. Gracia, I. Aldalur, H. B. Eitouni, M. Joost, M. Armand and H. Zhang, *Chem. Mater.*, 2022, **34**, 3451–3460.
25 L. Qiao, S. Rodriguez Peña, M. Martínez-Ibañez, A. Santiago, I. Aldalur, E. Lobato, E. Sanchez-Diez, Y. Zhang, H. Manzano, H. Zhu, M. Forsyth, M. Armand, J. Carrasco and H. Zhang, *J. Am. Chem. Soc.*, 2022, **144**, 9806–9816.
26 M. Zhou, K. Cui, T.-S. Wang, Z. Luo, L. Chen, Y. Zheng, B. Li, B. Shi, J. Liu, J.-J. Shao, G. Zhou, S. Yang and Y.-B. He, *ACS Nano*, 2024, **18**, 26986–26996.
27 Z. Luo, W. Li, C. Guo, Y. Song, M. Zhou, Y. Shi, J. Xu, L. Li, B. Shi, Q. Ouyang, J.-J. Shao and G. Zhou, *Particuology*, 2024, **85**, 146–154.
28 Y. V. Shevtsov, D. R. Nosov, A. S. Shaplov and D. F. Schmidt, LU601870 TFSI-functional thioether compounds for electrochemical applications, 2025.
29 H. T. Ho, M. Rollet, T. N. T. Phan and D. Gigmes, *Eur. Polym. J.*, 2018, **107**, 74–81.
30 X. Yang, M. Jiang, X. Gao, D. Bao, Q. Sun, N. Holmes, H. Duan, S. Mukherjee, K. Adair, C. Zhao, J. Liang, W. Li, J. Li, Y. Liu, H. Huang, L. Zhang, S. Lu, Q. Lu, R. Li, C. V. Singh and X. Sun, *Energy Environ. Sci.*, 2020, **13**, 1318–1325.
31 S. Porporato, J. L. Gómez-Urbano, A. Piovano, G. A. Elia, C. Gerbaldi and A. Balducci, *Electrochim. Acta*, 2025, **525**, 146096.
32 R.-S. Kühnel, M. Lübke, M. Winter, S. Passerini and A. Balducci, *J. Power Sources*, 2012, **214**, 178–184.